Monthly Notices of the ROYAL ASTRONOMICAL SOCIETY

MNRAS **523,** 1661–1675 (2023) https://doi.org/10.1093/mnras/stad1534
Advance Access publication 2023 May 22

Synchrotron emission from double-peaked radio light curves of the symbiotic recurrent nova V3890 Sagitarii

Miriam M. Nyamai [1,2★] Justin D. Linford [3] James R. Allison [4,5] Laura Chomiuk,[6★] Patrick A. Woudt [2★] Valério A. R. M. Ribeiro [7] and Sumit K. Sarbadhicary [8]

[1]*South African Radio Observatory (SARAO), 2 Fir Street, Black River Park, Observatory, Cape Town, 7925, South Africa*
[2]*Department of Astronomy, University of Cape Town, Private Bag X3, Rondebosch 7701, South Africa*
[3]*National Radio Astronomy Observatory, PO Box O, Socorro, NM, 87801, USA*
[4]*Sub-Deptartment of Astrophysics, Department of Physics, University of Oxford, Denys Wilkinson Building, Keble Rd., Oxford OX1 3RH, UK*
[5]*First Light Fusion Ltd, Unit 9/10 Oxford Industrial Park, Mead Road, Yarnton, Kidlington OX5 1QU, UK*
[6]*Center for Data Intensive and Time Domain Astronomy, Department of Physics and Astronomy, Michigan State University, East Lansing, MI 48824, USA*
[7]*Instituto de Telecomunicações, Campus Universitário de Santiago, P-3810-193 Aveiro, Portugal*
[8]*Center for Cosmology and AstroParticle Physics (CCAPP), The Ohio State University, 191 W. Woodruff Avenue, Columbus, OH 43210, USA*

Accepted 2023 May 16. Received 2023 May 16; in original form 2022 October 31

ABSTRACT

We present radio observations of the symbiotic recurrent nova V3890 Sagitarii following the 2019 August eruption obtained with the MeerKAT radio telescope at 1.28 GHz and Karl G. Janksy Very Large Array (VLA) at 1.26−35 GHz. The radio light curves span from day 1 to 540 days after eruption and are dominated by synchrotron emission produced by the expanding nova ejecta interacting with the dense wind from an evolved companion in the binary system. The radio emission is detected early on (day 6) and increases rapidly to a peak on day 15. The radio luminosity increases due to a decrease in the opacity of the circumstellar material in front of the shocked material and fades as the density of the surrounding medium decreases and the velocity of the shock decelerates. Modelling the light curve provides an estimated mass-loss rate of $\dot{M}_{\rm wind} \approx 10^{-8}$ M$_\odot$ yr^{-1} from the red giant star and ejecta mass in the range of $M_{\rm ej} = 10^{-5}$—10^{-6} M$_\odot$ from the surface of the white dwarf. V3890 Sgr likely hosts a massive white dwarf similar to other symbiotic recurrent novae, thus considered a candidate for supernovae type Ia (SNe Ia) progenitor. However, its radio flux densities compared to upper limits for SNe Ia have ruled it out as a progenitor for SN 2011fe like supernovae.

Key words: radio continuum: transients – novae, cataclysmic variables – stars: individual: V3890 Sgr – acceleration of particles.

1 INTRODUCTION

V3890 Sgr belongs to a class of cataclysmic variables known as symbiotic recurrent novae; 'symbiotic' because the accreting white dwarf has a giant companion (e.g. Schaefer 2010). It is a recurrent nova because more than one thermonuclear eruption has been observed from this system; the most recent eruption occurred on 2019 August 27.9 UT as reported by A. Pereira (Strader et al. 2019; Kafka 2020). Previous eruptions of the nova were observed in 1962 June (Wenzel 1990; Miller 1991) and 1990 April 27.7 (e.g. Buckley et al. 1990; Anupama & Sethi 1994).

Initially, the orbital period of V3890 Sgr was estimated as 519.7 days (Schaefer 2009). However, recently using optical observations, Mikołajewska et al. (2021) estimated an orbital period of 747.6 days for V3890 Sgr. The nova is, therefore, in the same class as other long-period recurrent novae such as RS Oph, V745 Sco, T CrB, and V2487 Oph (Anupama & Mikołajewska 1999; Schaefer 2009, 2010). Since some of the symbiotic recurrent novae have been extensively studied, their known parameters are listed in Table 1 and compared with V3890 Sgr.

The optical light curves of these recurrent symbiotic novae evolve quickly following an eruption due to the low mass of material accreted onto the surface of the white dwarf since the last nova eruption, as these systems are known to host massive white dwarfs ($\gtrsim 1.2$ M$_\odot$; see Table 1). The ejecta outflows following an eruption are also fast, with velocities $\gtrsim 4000$ km s^{-1} measured from emission lines observed during different stages of the spectral evolution (see Table 1). The emission lines, however, become narrower with time during the early phase of the ejecta evolution, as the nova ejecta sweep up and are decelerated by the wind from the secondary star (e.g. Gonzalez-Riestra 1992; Banerjee et al. 2014; Mondal et al. 2018).

Recurrent novae have short recurrence times of less than a century (see Table 1), which are attributed to high accretion rates, $\dot{M} \approx 10^{-8}$ $M_\odot$ yr^{-1} (Yaron et al. 2005). The high rates rapidly supply enough material to power the subsequent thermonuclear runaway. Theoretically, most recurrent novae also consist of massive white dwarfs, and therefore require less mass to accumulate for hydrogen ignition (e.g. Prialnik & Kovetz 1995; Yaron et al. 2005; Wolf et al. 2013). In symbiotic systems, the high $\dot{M}$ is acquired through mass-loss from the companion red giant, which is accreted either as a wind or through a disc via the inner Lagrangian point (Luna

★ E-mail: nymmir001@myuct.ac.za(MN); chomiukl@msu.edu(LC); pwoudt@ast.uct.ac.za(PW)

Table 1. Estimated parameters of the symbiotic recurrent novae based on multiwavelength studies of individual systems. Listed parameters include masses of the binary components, the spectral classification of the companion star, orbital period ($P_{\rm orbit}$), years of recorded eruptions, the nova recurrence time ($t_{\rm rec}$), velocity of the ejected material ($V_{\rm ej}$), the time it takes for the nova to fade from optical maximum by three magnitudes (t_3), and the distance to the nova (d).

Name	$M_{\rm white\ dwarf}$ $M_\odot$	$M_{\rm giant}$ $M_\odot$	Spectral type	$P_{\rm orbit}$ (Days)	Years of eruption	$t_{\rm rec}$ (yrs)	$V_{\rm ej}$ (km s^{-1})	t_3 (Days)	d (kpc)
T CrB	1.37 (1)	1.12 (1)	M4 III (2)	228 (3)	1866, 1946	80		6 (8)	0.81 (4)
RS Oph	1.2–1.4 (5)	0.7–0.8 (5)	M0–2 III (6)	453.6 (5)	1898, 1907, 1933, 1945, 1958, 1967, 1985, 2006, 2021	$\gtrsim 10$	4200 (7)	14 (8)	1.6 (9)
V745 Sco			M4 III (10)	510 (8)	1937, 1963, 1989, 2014	25	> 4000 (11)	9 (8)	7.8 (8)
V3890 Sgr	1.35 (12)	1.1 (12)	M5 III (10)	747.6 (12)	1962, 1990, 2019	28	$\gtrsim 4200$ (13)	14 (8)	9 (12)

Note. References: (1) Stanishev et al. (2004), (2) Mürset & Schmid (1999), (3) Kenyon & Garcia (1986), (4) Bailer-Jones et al. (2018), (5) Brandi et al. (2009), (6) Anupama & Mikołajewska (1999), (7) Mondal et al. (2018), (8) Schaefer (2010), (9) Hjellming et al. (1986), (10) Harrison, Johnson & Spyromilio (1993), (11) Banerjee et al. (2014), (12) Mikołajewska et al. (2021), (13) Strader et al. (2019), and (14) Munari & Walter (2019b).

2019). The mass-loss via the giant's wind also contributes to a dense circumstellar environment, which is impacted by the expanding nova envelope to give rise to shocks observed at high energies such as X-rays (e.g. Bode & Kahn 1985; Sokoloski et al. 2006) and γ-rays (Zheng et al. 2022). A combination of high-mass white dwarfs and high-mass accretion rates make the eruptions of these systems relatively gentle, and consequently not all of the accreted material is ejected during eruption (Yaron et al. 2005). The white dwarf may therefore grow in mass towards the Chandrasekhar limit. Indeed, the white dwarfs in recurrent novae have been shown to be massive (Osborne et al. 2011; Page et al. 2015), and these systems have therefore been proposed as progenitors of supernovae type Ia (Maoz, Mannucci & Nelemans 2014). However, it is not clear whether the underlying white dwarfs in recurrent symbiotic novae are composed of CO or ONe. A CO white dwarf is required for a SN Ia; the fate of an ONe white dwarf that has grown in mass towards the Chandrasekhar limit is instead an accretion-induced collapse into a neutron star (Gutierrez et al. 1996).

Based on previous eruptions, the optical evolution of V3890 Sgr is fast, taking less than a day to rise to maximum magnitude ($V \approx$ 8 mag) and 14 days for the brightness to drop by 3 mag; it is therefore classified as a fast nova (Payne-Gaposchkin 1964; Schaefer 2010).

The spectral evolution of V3890 Sgr at ultraviolet wavelengths shows the presence of both broad and narrow emission lines (Gonzalez-Riestra 1992). The broad lines originate from the expanding nova ejecta, while the narrow lines represent the speed of the red giant wind (e.g. Munari 2019). The FWHMs of the hydrogen Balmer lines decrease with time, from 2140 km s^{-1} to 210 km s^{-1} within a period of 13 days following the eruption in 1990 (Gonzalez-Riestra 1992). Following the 2019 eruption, the nova was observed with the Gemini observatory to obtain near-infrared spectra during the early days after the outburst (Evans et al. 2022). During this time, Helium emission lines showed both broad and narrow components. The broad lines emerged on day 3 and narrowed through day 23 (Evans et al. 2022). This is interpreted as evidence of the high-velocity nova envelope being decelerated with time as it sweeps up the red giant wind.

The rise, peak, and decay of the optical light curve of V3890 Sgr following the 2019 August eruption is well observed (Sokolovsky et al. 2019; Strader et al. 2019). The optical evolution of the nova shown in Fig. 1 is similar to previous outbursts (see Fig. 1).

The eruption has been observed at γ-ray, X-ray, infrared, UV, optical, and radio wavelengths (Buson, Jean & Cheung 2019; Nyamai et al. 2019; Polisensky et al. 2019; Orio et al. 2020; Evans et al. 2022; Kaminsky et al. 2022; Ness et al. 2022). V3890 Sgr was

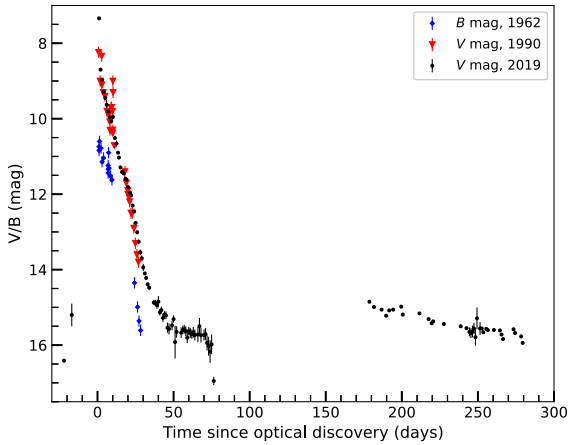

Figure 1. The V-band and B-band optical light curves of the 1962, 1990, and 2019 eruptions of V3890 Sgr from AAVSO data (Kafka 2020) and data presented by Schaefer (2010). Here we set t_0 to time of the eruptions (Sokolovsky et al. 2019).

detected in γ-rays and hard X-rays very soon ($\sim$2 days) following the eruption (Buson et al. 2019; Sokolovsky et al. 2019), consistent with expectations for a nova erupting in a dense environment.

Presented in this paper are radio observations of V3890 Sgr with MeerKAT at 1.28 GHz and the VLA at radio frequencies between 1.26 GHz and 35 GHz. The observations are used to study the transient phenomena of the system at radio frequencies. In Section 2, radio observations and measurements including the radio light curve, radio spectral evolution, and H I absorption analysis are presented. The emission from the nova, modelled as synchrotron radiation emanating from the interaction of the ejecta with the red giant wind, is analysed in Section 3. The conclusions are highlighted in Section 4.

2 RADIO OBSERVATIONS

2.1 MeerKAT and VLA observations of V3890 Sgr

Monitoring of V3890 Sgr with the MeerKAT telescope started on $(t - t_0) \approx 2$ days, where t_0 is taken as 2019 August 27.9 (MJD 58722.9). V3890 Sgr is the first recurrent nova to be studied with MeerKAT. MeerKAT is a radio telescope located in South Africa and consists of 64 dishes each with a diameter of 13.5 m (Jonas & MeerKAT Team 2016). Combined, they form an array with a maximum baseline of 8 km. The observations were taken using the MeerKAT L-band receiver, which has a total bandwidth of 856 MHz split into 4096 channels each with a width of 209 kHz. The

frequency range covered is 0.9 to 1.67 GHz centred at 1.284 GHz. In each observation, the time on target was between 15 and 30 min (see Table 2). For the first 15 days after optical discovery, V3890 Sgr was observed daily and then every 2 days afterwards until day 25. Later, the observations were carried out once every week and finally the cadence was slowed down further to twice every month until the end of the observations on 2020 May 26. For all the epochs, the flux and bandpass calibrator J1939-6342 was observed for ∼5 mins. The complex gain (secondary) calibrator J1911-2006 was observed for 2 min per visit before and after observing the target.

V3890 Sgr was observed with the VLA from 2019 August 30 to 2021 February 13 at observing frequencies between 1 GHz and 37 GHz. Observations were conducted using the *L*, *C*, *Ku*, and *Ka* band receivers. The total bandwidth was 1 GHz for *L* band (1–2 GHz), 4 GHz for *C* band (4–8 GHz), 6 GHz for Ku band (12–18 GHz), and 8 GHz for *Ka* band (28.5–32.5 and 34.0–38.0 GHz). For all epochs, the absolute flux density and bandpass calibrator 3C286 was observed for 2 min per band. The complex gain calibrator J1820-2528 was used for all observations at *C*, *Ku*, and *Ka* bands. For the *L* band observations, the complex gain calibrator was J1820-2528 during A and B configurations, and J1833-2103 during C and D configurations. VLA observations were carried out under programs VLA/19B-313 and VLA/20B-302. The total observing time on target aross all frequency bands varied between 17 mins and 78 mins (see Table 2).

2.2 Data reduction

Data reduction for MeerKAT was undertaken using `CASA` (McMullin et al. 2007). To remove radio-frequency interference, the data were flagged using the `AOflagger` algorithm (Offringa, van de Gronde & Roerdink 2012). In order to find the bandpass corrections, first the phase-only and antenna-based delay corrections were determined on the primary calibrator. The primary calibrator bandpass corrections were then applied. This was followed by solving for complex gains for both the primary and secondary calibrators. The absolute flux density of the secondary calibrator was estimated by scaling the corrections from the primary to the secondary calibrator. Calibrations and the absolute flux-density scale were consequently transferred to V3890 Sgr (the target).

Imaging of MeerKAT data was performed using `WSCLEAN` (Offringa et al. 2014) using a Briggs weighting with a robust value of −0.7. These steps are summarized in the oxkat pipeline.[1] The flux densities of V3890 Sgr were estimated with the `CASA IMFIT` task by fitting a Gaussian to the image of the target. Since the nova was very bright, exhibiting a high signal-to-noise ratio, the width of the Gaussian was allowed to vary when obtaining the flux density measurements. For non-detections, the upper limit was calculated as the pixel value at the location of the nova added to 3 × rms value of a region in the image away from the target location. The observations and results are presented in Table 3 and plotted in Fig. 2. The quoted errors on the flux densities include Gaussian fit errors ($\sigma_{\rm Fit}$) and 10 per cent calibration errors ($\sigma_{\rm cal} = 0.1 S_\nu$; e.g. Hewitt et al. 2020) such that

$$\sigma_{S_\nu} = \sqrt{\sigma^2_{\rm Fit} + (0.1 \times S_\nu)^2}. \quad (1)$$

[1]https://www. github.com/IanHeywood/oxkat and through the Astrophysics Source Code Library record ascl:2009.003 (Heywood 2020).

The VLA data were calibrated using the VLA `CASA` calibration pipeline versions 5.4.2 and 5.6.2. Additional flagging was done in `AIPS` (Greisen 2003) and final imaging was done using `Difmap` (Shepherd 1997). The VLA data for each band were split into two subbands for imaging to increase spectral coverage. When possible, phase self-calibration was performed in `Difmap` as part of the imaging process. All images where the nova was detected were then loaded into `AIPS` and flux density measurements were made using the `JMFIT` task. As with the MeerKAT data, we include 10 per cent calibration uncertainty for the VLA flux density values, added in quadrature with the statistical uncertainty from `JMFIT`. In the cases of non-detections, we recorded the flux density value at the location of the nova and obtained the image rms in a region away from the nova. The upper limit values presented for the VLA are the flux density value at the nova location plus 3 × the off-source image rms.

2.3 Radio light curve

The 1 to 37 GHz light curves are plotted in Fig. 2. Initially, during day 2 to day 5 after eruption, the nova was not detected, with 3σ upper limits of <0.2 mJy. V3890 Sgr then shows a rapid increase in flux density, which peaked first on day 19 and again on day 60, forming a double peaked radio light curve. The flux density varies with frequency, such that the light curve peaks first at higher frequencies (> 5 GHz). During this time, the flux is still rising at lower frequencies (< 2 GHz), which peak later. During the first peak, (day 19), the brightness of the nova remains the same at all observed frequencies. However, during the second peak, (day 60), the nova is brighter at lower frequencies. After the secondary peak, the nova faded to flux densities below 0.1 mJy.

2.4 Radio spectral evolution

To determine the spectral evolution of V3890 Sgr, the data are fit assuming a simple power law using the method of least-squares. Measurements of the spectral index (α where $S_\nu \propto \nu^\alpha$) are presented in Figs 2 and 3. During the early times (e.g. on day 11.2), the flux density rises towards higher frequency, giving $\alpha = 0.29$, an indicator of optically thick emission. Around the radio light curve maximum, e.g. on day 21 the spectrum switches to rising towards lower frequency, and is well described by a power law with slope $\alpha = -0.2$.

The spectrum continues to steepen (α becomes more negative,) with time, as shown on day 67 where $\alpha = -0.4$. On day 327, the spectrum appears to flatten ($\alpha = -0.1$), which could indicate some contribution from optically thin free–free emission. However, the flux densities on day 327 were quite low with significant uncertainty at the lowest and highest frequencies. Also, on day 534, the spectrum rises steeply again towards lower frequencies and can be fit with a single power law such that $\alpha = -0.6$, an indication of optically thin synchrotron emission. A mixture of optically thin free–free emission and synchrotron emission has also been observed in other novae such as V445 Pup (Nyamai et al. 2021) and V1535 Sco (Linford et al. 2017).

2.5 H I 21-cm absorption measurements towards V3890 Sgr

The distance to V3890 Sgr is not well constrained, with estimates ranging from 4.4 kpc to 9.0 kpc using different methods (Schaefer 2010; Munari & Walter 2019a; Orio et al. 2020; Mikołajewska et al. 2021). Following the latest eruption, Munari & Walter (2019a)

Table 2. A summary of MeerKAT and VLA observations of V3890 Sgr.

Observation Date	t (MJD)	$t - t_0$ (Days)	Observation frequency (GHz)	Telescope	Observation time (mins)
2019 August 29	58724.8	1.9	1.28	MeerKAT	30.0
2019 August 30	58725.7	2.8	1.28	MeerKAT	30.0
2019 August 30	58726.0	3.1	5.0, 7.0	VLA (A configuration)	18.0
2019 August 31	58726.8	3.9	1.28	MeerKAT	30.0
2019 September 01	58727.8	4.9	1.28	MeerKAT	30.0
2019 September 02	58728.8	5.9	1.28	MeerKAT	30.0
2019 September 03	58729.8	6.9	1.28	MeerKAT	30.0
2019 September 04	58730.0	7.2	1.26, 1.78, 5.0, 7.0	VLA (A configuration)	18.0
2019 September 04	58730.9	8.0	1.28	MeerKAT	30.0
2019 September 05	58731.0	8.1	1.26, 1.78, 5.0, 7.0	VLA (A configuration)	18.0
2019 September 05	58731.9	8.5	1.28	MeerKAT	30.0
2019 September 06	58732.9	9.5	1.28	MeerKAT	30.0
2019 September 07	58733.6	10.4	1.28	MeerKAT	30.0
2019 September 08	58734.1	11.2	1.26, 1.78, 5.0, 7.0	VLA (A configuration)	17.0
2019 September 08	58734.6	11.7	1.28	MeerKAT	30.0
2019 September 09	58735.8	12.9	1.28	MeerKAT	15.0
2019 September 11	58737.0	14.1	1.26, 1.78, 5.0, 7.0	VLA (A configuration)	17.0
2019 September 11	58737.8	14.9	1.28	MeerKAT	15.0
2019 September 13	58739.0	16.1	1.26, 1.78, 5.0, 7.0	VLA (A configuration)	17.0
2019 September 13	58739.9	17.0	1.28	MeerKAT	15.0
2019 September 15	58741.8	18.9	1.28	MeerKAT	15.0
2019 September 17	58743.9	21.0	1.28	MeerKAT	15.0
2019 September 18	58744.1	21.2	1.26, 1.78, 5.0, 7.0	VLA (A configuration)	17.0
2019 September 19	58745.8	22.9	1.28	MeerKAT	15.0
2019 September 21	58747.6	24.7	1.28	MeerKAT	15.0
2019 September 22	58749.0	26.1	1.26, 1.78, 5.0, 7.0	VLA (A configuration)	17.0
2019 September 24	58751.0	28.1	1.26, 1.78, 5.0, 7.0	VLA (A configuration)	17.0
2019 September 26	58752.7	29.8	1.28	MeerKAT	15.0
2019 September 29	58755.7	32.8	1.28	MeerKAT	15.0
2019 September 30	58756.9	34.0	1.26, 1.78, 5.0, 7.0	VLA (A configuration)	17.0
2019 October 04	58761.0	38.1	1.26, 1.78, 5.0, 7.0	VLA (A configuration)	17.0
2019 October 06	58762.7	39.8	1.28	MeerKAT	15.0
2019 October 08	58765.0	42.1	1.26, 1.78, 5.0, 7.0	VLA (A configuration)	17.0
2019 October 11	58768.0	45.0	1.26, 1.78, 5.0, 7.0	VLA (A configuration)	17.0
2019 October 17	58774.0	51.1	1.26, 1.78, 5.0, 7.0	VLA (A configuration)	17.0
2019 October 26	58782.6	59.7	1.28	MeerKAT	20.0
2019 November 02	58790.0	67.0	1.26, 1.78, 5.0, 7.0, 13.5, 16.5, 29.5, 35.0	VLA (A configuration)	40.6
2019 November 18	58805.7	82.8	1.28	MeerKAT	20.0
2019 November 18	58806.8	83.9	1.26, 1.78, 5.0, 7.0	VLA (D configuration)	17.0
2019 November 23	58810.9	88.0	13.5, 16.5, 29.5, 35.0	VLA (D configuration)	24.3
2019 November 30	58817.6	94.7	1.28	MeerKAT	20.0
2019 December 10	58827.8	104.9	1.26, 1.78, 5.0, 7.0, 13.5, 16.5, 29.5, 35.0	VLA (D configuration)	37.9
2019 December 13	58830.6	107.7	1.28	MeerKAT	20.0
2020 January 04	58852.8	129.8	5.0, 7.0, 13.5, 16.5, 29.5, 35.0	VLA (D configuration)	37.9
2020 February 26	58905.5	182.6	1.26, 1.74, 13.5, 16.5, 29.5, 35.0	VLA (D configuration)	37.9
2020 March 24	58932.1	209.2	1.28	MeerKAT	15.0
2020 April 08	58947.4	224.5	1.26, 1.74, 13.5, 16.5, 29.5, 35.0	VLA (C configuration)	37.9
2020 April 14	58953.0	230.1	1.28	MeerKAT	15.0
2020 May 18	58988.0	265.1	1.28	MeerKAT	15.0
2020 May 21	58990.3	267.4	1.26, 1.78, 13.5, 16.5, 29.5, 35.0	VLA (C configuration)	37.9
2020 May 26	58995.2	272.3	1.28	MeerKAT	15.0
2020 July 20	59050.2	327.3	1.26, 1.78, 13.5, 16.5, 29.5, 35.0	VLA (B configuration)	38.6
2020 October 06	59128.0	405.1	1.26, 1.78, 13.5, 16.5, 29.5, 35.0	VLA (B configuration)	44.5
2021 February 13	59258.6	535.7	1.26, 1.78, 5.0, 7.0	VLA (A configuration)	78.4

Note. Here, t_0 is taken as 2019 August 27.9 UT (MJD $= 58722.9$).

determined a reddening of $E(B - V) = 0.56$ mag using absorption features of optical spectral lines. Comparing this value with the three-dimensional interstellar reddening maps of Green et al. (2019) and Lallement et al. (2014), they estimate a distance of >4.5 kpc. Using the surface temperature and the size of the companion star, a black body distance of 7 kpc is derived to the nova (Schaefer 2010). This method relies on the orbital period of the system and assumes that the companion star fills its Roche lobe (which is far from certain in the case of a symbiotic binary).

Since estimates of the distance to V3890 Sgr vary based on different observations, an attempt is made here to further constrain the distance using H I absorption along the line-of-sight

Table 3. A summary of the radio flux densities of V3890 Sgr from MeerKAT and VLA observations.

$t - t_0$ (Days)	S_1.28 (mJy)	S_1.26 (mJy)	S_1.78 (mJy)	S_5.0 (mJy)	S_7.0 (mJy)	$S_1$3.5 (mJy)	$S_1$6.5 (mJy)	$S_2$9.5 (mJy)	$S_3$5.0 (mJy)	Spectral index (α)
1.9	< 0.15									
2.8	< 0.18									
3.1				0.79 ± 0.04	2.35 ± 0.12					
3.9	< 0.19									
4.9	< 0.18									
5.9	0.62 ± 0.06									
6.9	3.22 ± 0.32									
7.2		3.73 ± 0.21	13.94 ± 0.70	43.48 ± 2.17	44.62 ± 2.23					1.30 ± 0.35
8.0	8.03 ± 0.80									
8.1		9.06 ± 0.46	21.10 ± 1.06	46.09 ± 2.31	46.17 ± 2.31					0.90 ± 0.22
8.5	12.53 ± 1.25									
9.5	18.65 ± 1.87									
10.4	24.08 ± 2.41									
11.2		28.30 ± 1.42	40.97 ± 2.05	51.11 ± 2.56	48.93 ± 2.45					0.29 ± 0.11
11.7	32.03 ± 3.21									
12.9	40.44 ± 4.05									
14.1		44.15 ± 2.21	48.95 ± 2.45	48.74 ± 2.44	44.35 ± 2.22					0.00 ± 0.05
14.9	44.20 ± 4.42									
16.1		44.67 ± 2.24	46.26 ± 2.31	44.01 ± 2.20	39.89 ± 2.00					-0.06 ± 0.03
17.0	43.0 ± 4.30									
18.9	44.07 ± 4.41									
21.0	43.35 ± 4.34									
21.2		44.66 ± 2.24	42.95 ± 2.15	36.23 ± 1.81	31.92 ± 1.60					-0.19 ± 0.02
21.9	42.68 ± 4.27									
24.7	39.18 ± 3.92									
26.1		38.89 ± 1.95	34.18 ± 1.71	27.12 ± 1.36	23.49 ± 1.18					-0.28 ± 0.02
28.1		35.30 ± 1.77	31.10 ± 1.56	24.83 ± 1.24	21.18 ± 1.06					-0.28 ± 0.03
29.8	32.49 ± 3.25									
32.8	30.88 ± 3.10									
34.0		31.53 ± 1.58	26.97 ± 1.35	21.19 ± 1.06	17.24 ± 0.86					-0.32 ± 0.04
38.1		30.85 ± 1.54	25.99 ± 1.30	19.96 ± 1.00	16.36 ± 0.82					-0.34 ± 0.04
39.8	29.84 ± 2.99									
42.1		30.09 ± 1.51	25.30 ± 1.27	18.95 ± 0.95	15.48 ± 0.77					-0.36 ± 0.03
45.0		30.41 ± 1.52	25.55 ± 1.28	18.68 ± 0.93	15.28 ± 0.76					-0.38 ± 0.03
51.1		29.53 ± 1.48	24.62 ± 1.23	17.29 ± 0.86	13.94 ± 0.70					-0.41 ± 0.03
59.7	26.04 ± 2.61									
67.0		22.26 ± 1.12	19.21 ± 0.96	12.38 ± 0.62	10.17 ± 0.51	7.54 ± 0.75	7.17 ± 0.72	6.01 ± 0.60	5.99 ± 0.60	-0.42 ± 0.01
82.8	15.76 ± 1.58									
83.9		12.39 ± 1.19	12.19 ± 0.69	7.81 ± 0.39	6.68 ± 0.34					-0.40 ± 0.04
88.0						4.62 ± 0.46	4.40 ± 0.44	3.49 ± 0.35	3.18 ± 0.32	-0.39 ± 0.03
94.7	11.56 ± 1.16									
104.9		8.94 ± 0.74	7.46 ± 0.45	4.0 ± 0.20	3.9 ± 0.20	3.22 ± 0.32	3.08 ± 0.31	2.04 ± 0.21	1.93 ± 0.20	-0.44 ± 0.03
107.7	8.08 ± 0.81									
129.8				2.45 ± 0.13	2.26 ± 0.12	1.78 ± 0.18	1.73 ± 0.17	1.45 ± 0.15	1.28 ± 0.13	-0.32 ± 0.01
182.6		2.05 ± 0.32	1.18 ± 0.14	0.83 ± 0.04	0.80 ± 0.04	0.72 ± 0.07	0.66 ± 0.07	0.55 ± 0.06	0.59 ± 0.07	-0.28 ± 0.05
209.2	1.01 ± 0.11									
224.5		1.54 ± 0.08	0.36 ± 0.14	0.38 ± 0.02	0.44 ± 0.03	0.39 ± 0.04	0.35 ± 0.04	0.35 ± 0.05	0.28 ± 0.04	-0.10 ± 0.06
230.1	0.79 ± 0.08									
265.1	0.42 ± 0.06									
267.4		<1.38	< 0.55	0.27 ± 0.02	0.27 ± 0.02	0.23 ± 0.03	0.22 ± 0.14	0.15 ± 0.03	0.13 ± 0.03	-0.32 ± 0.07
272.3	0.42 ± 0.05									
327.3		< 0.40	0.21 ± 0.05	0.17 ± 0.02	0.14 ± 0.02	0.14 ± 0.02	0.13 ± 0.02	0.16 ± 0.04	0.17 ± 0.05	-0.11 ± 0.07
405.1		< 0.35	< 0.55	0.14 ± 0.02	0.10 ± 0.02	0.09 ± 0.01	0.09 ± 0.01	< 0.19	< 0.21	-0.41 ± 0.11
535.7		<0.18	0.10 ± 0.02	0.05 ± 0.01	0.04 ± 0.01					-0.63 ± 0.01

Note. Here, t_0 is taken as 2019 August 27.9 UT (MJD $= 58722.9$).

to the nova (see Chauhan et al. 2021 for more details about H I absorption with MeerKAT). The epochs used to obtain the H I spectrum towards V3890 Sgr include radio detections of the nova when it was at its brightest (>30 mJy). Fig. 4 shows the average MeerKAT H I spectrum towards V3890 Sgr, compared with the average of seven reference sources (indicated by the blue spectrum in Fig. 4) that have been offset for clarity. These reference sources are presumably background extragalactic sources, and their spectra were averaged together to yield optimal S/N. These spectra were constructed by taking an inverse-variance weighted average over spectra from seven epochs observed with MeerKAT. Line-of-sight absorption through Galactic H I clouds is detected towards V3890 Sgr. By identifying distinct kinematic components in the H I spectrum, and comparing with the spectrum of reference sources, an attempt is made to determine the distance to V3890 Sgr.

H I absorption at the level of 12 per cent is clearly detected in both the spectra of V3890 Sgr and the reference sources. In both cases, the absorption is at a velocity of 14 ± 22 km s^{-1}, but is unfortunately unresolved by the data obtained in the MeerKAT 4k correlator mode. At the time of the observations, the 32k correlator mode was not yet available. Absorption is detected at velocities

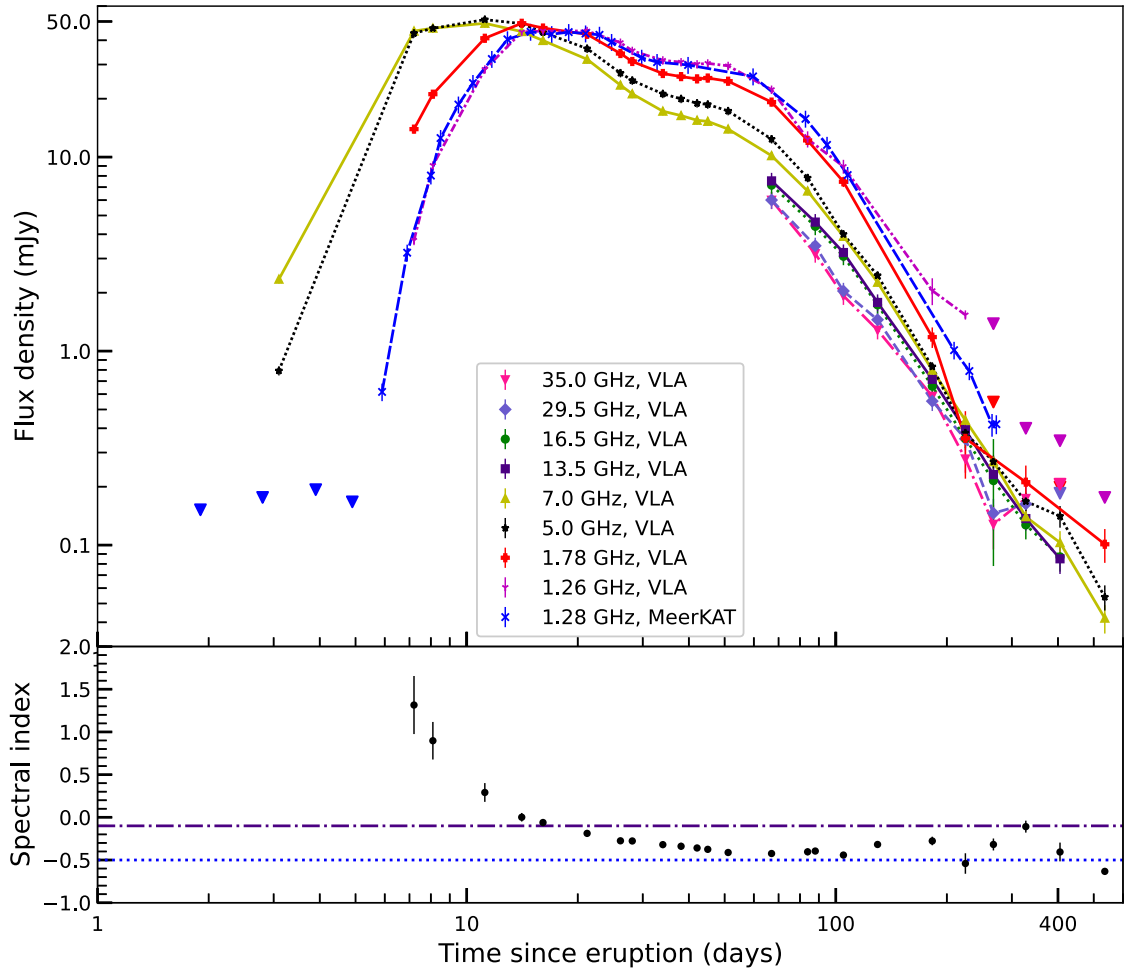

Figure 2. Top: Observed flux densities of V3890 Sgr spanning from day 2 to day 536 after the nova eruption. The upper limits in flux density are included as triangles. We take MJD $= 58722.9$ as the date of the eruption (t_0). Bottom: spectral indices obtained by fitting a single power-law to multiband data (1.26–35) GHz. The dash-dotted line in the lower panel represents $\alpha = -0.1$, the theoretically expected index of optically thin free–free emission. The dotted line represents $\alpha = -0.5$, the expected index of optically thin synchrotron emission.

lower than 36 km s^{-1}, corresponding to kinematic distances greater than $4.44^{+0.34}_{-0.31}$ kpc (using a Monte Carlo technique by Wenger et al. 2018). This estimate is similar to the distance value obtained using interstellar reddening as discussed earlier. Therefore, the distance constraint for this nova is consistent with being greater than 4.4 kpc. The absolute magnitude in the *V* filter and bolometric magnitude measurements give distance estimates of 8.75 and 9 kpc, respectively (Mikołajewska et al. 2021). A distance of 9 kpc is thus adopted for calculations in this work.

3 DISCUSSION

3.1 Radio emission from V3890 Sgr is synchrotron-dominated

The radio emission of novae embedded in the winds of giant stars is dominated by synchrotron emission, as observed in systems such as RS Oph (Taylor et al. 1989; O'Brien et al. 2006; Rupen, Mioduszewski & Sokoloski 2008; Sokoloski, Rupen & Mioduszewski 2008; Eyres et al. 2009), V745 Sco (Kantharia et al. 2016), and V1535 Sco (Linford et al. 2017). The non-thermal radio emission is the result of the ejecta interacting with the pre-existing circumstellar medium. A nova shock wave moving outwards populates a thin region of shocked circumstellar material with accelerated particles required for non-thermal emission. The evolution of the shock wave in symbiotic novae is similar to that of supernovae (SNe) following an explosion (e.g. Chevalier 1982b; O'Brien et al. 2006). The radio luminosity increases as the optically thick emitting region expands. As the emitting region expands, the free–free optical depth from the ionized red giant wind ahead of the shock decreases, and the emission becomes optically thin. The radio luminosity peaks when $\tau = 1$, and then decays as the expanding shock wave decelerates in velocity and the surrounding medium drops in density (Chevalier 1982b).

The radio light curve of V3890 Sgr evolves through the three phases of rise, peak, and decay within months following the nova eruption, and is similar to V745 Sco (e.g. Kantharia et al. 2016). The radio spectra of V3890 Sgr during the rise phase of the light curve yield a spectral index of $\alpha \approx 1.3$, consistent with optically thick emission. After the radio peak, the spectral index is steep and converges to $\alpha = -0.3$ at late times of light curve evolution (see Fig. 2 and Table 3), an indication of optically thin synchrotron emission. Similar values of α are observed in sources that are strong synchrotron emission emitters such as SNe and SN remnants (Weiler et al. 2002; Green et al. 2019) and the helium nova V445 Pup (Nyamai et al. 2021).

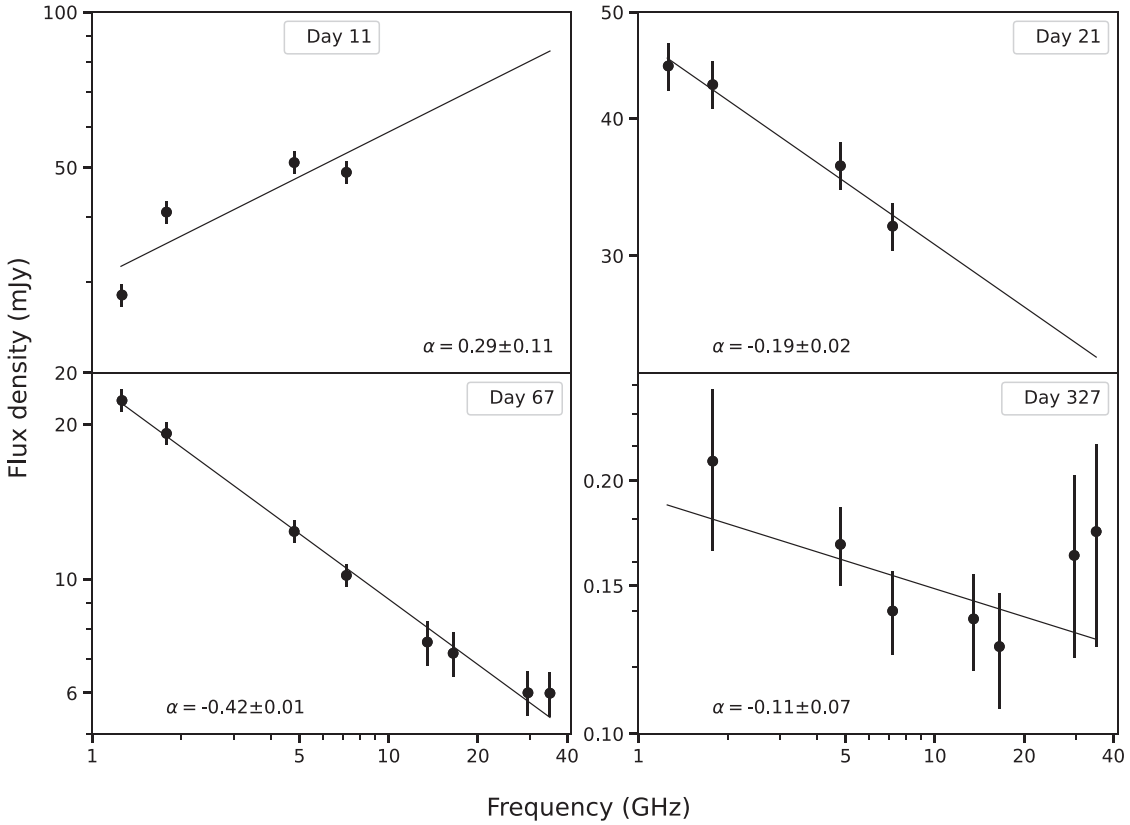

Figure 3. Spectral evolution of V3890 Sgr after the 2019 eruption. The time since eruption and α is given for each fit represented by a solid line.

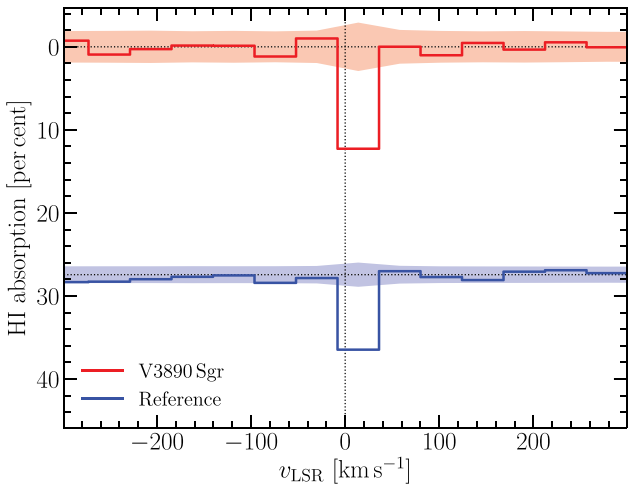

Figure 4. H I absorption spectrum showing an absorption between -8 km s^{-1} and 36 km s^{-1} with respect to the local standard of rest. The spectrum of V3890 Sgr is plotted in red colour and compared to an averaged spectrum of reference sources in blue colour. The shaded regions denote the noise level at 3σ.

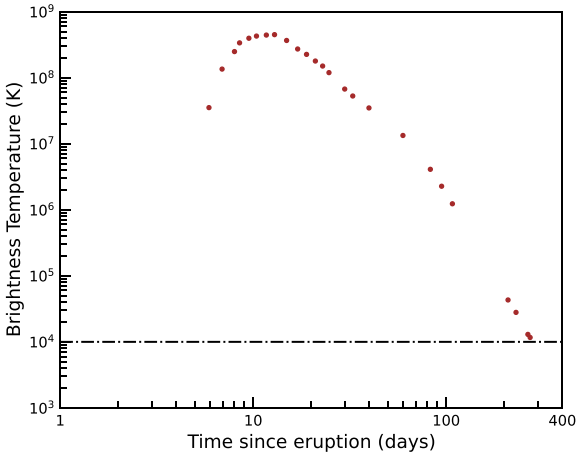

Figure 5. Brightness temperature of V3890 Sgr following the 2019 eruption, estimated assuming a constant shock velocity of 4200 km s^{-1}, a distance of 9 kpc to the nova and flux densities determined at 1.28 GHz observing frequency. The actual radius of the emitting region is less than the calculated shock radius since the shock is decelerating as it interacts with the red giant wind. Consequently, the brightness temperatures derived by assuming a constant shock velocity are lower limits.

To further constrain the type of emission from V3890 Sgr, the brightness temperature is determined by estimating the size of the emitting region (Nyamai et al. 2021; Chomiuk et al. 2021b). To determine the angular size of the emitting region, a spherically symmetric shock wave expanding at ≈ 4200 km s^{-1} since t_0 is assumed (Strader et al. 2019). Using flux densities observed at 1.28 GHz (23 cm), the estimated brightness temperatures on the first 200 days are $\gg 10^5$ K as shown in Fig. 5, a strong indicator of non-thermal emission (Chomiuk et al. 2021b). The brightness temperature after day 200 declines to $\approx 10^4$ K. However, we note that the actual angular size of the emitting region may be substantially smaller than our estimated size of the emitting region, since the shock wave decelerates as it interacts with the red giant wind. The implication

is that the brightness temperatures shown in Fig. 5 are lower limits. The spectral evolution and brightness temperatures indicate that the radio emission from V3890 Sgr is synchrotron-dominated, produced in a manner similar to that in SNe, where the radio light curve also evolves on time-scales of weeks to months (Weiler et al. 2002).

3.2 A model for synchrotron emission from nova blast waves

In an environment where the nova ejecta interact with a dense surrounding medium, radio emission can be used to probe the external surrounding medium and determine its density profile, as is commonly done in radio SNe (e.g. Weiler et al. 2002). The radial profile depends on the mass-loss from the companion star and its shaping by binary interaction (e.g. Ji et al. 2013; Mohamed et al. 2015). An interaction of the nova ejecta with the companion's wind will accelerate particles to high energies through diffusive shock acceleration (Bell 1978; Blandford & Ostriker 1978) and amplify the shock magnetic field (Bell 2004), producing synchrotron radiation. The interaction produces a forward shock, which drives into the pre-existing circumstellar material and a reverse shock driving into the ejecta (Chevalier 1982a; Reynolds 2017). The radius of discontinuity $R_{\rm cd}$ separates the forward- and reverse-shocked regions. The evolution of the shock fronts depends on the density structure of the nova ejecta ($\rho_{\rm ej}$) and that of the surrounding medium ($\rho_{\rm CSM}$; Chevalier 1982a; Tang & Chevalier 2017).

To interpret the radio luminosity from V3890 Sgr, this double shock system is considered. Shock wave dynamics have been observed in X-rays for recurrent novae, where the most notable characteristics of the shocked ejecta are high temperatures, $\gtrsim 10^7$ K, which decrease with time as the shock decelerates (e.g. Bode et al. 2006; Sokoloski et al. 2006). Immediately following its 2019 eruption, V3890 Sgr produced hard X-rays that were attributed to the nova outflow impacting the red-giant wind (Sokolovsky et al. 2019; Orio et al. 2020; Page et al. 2020; Singh et al. 2021). More evidence of shocks in V3890 Sgr comes from the presence of high-ionization emission lines in optical and infrared spectra (Munari & Walter 2019b; Evans et al. 2022).

A formalism for predicting synchrotron emission from shocks is put forward by Chevalier (1982b). Above a minimum energy $E_{\rm min}$, the energy spectrum of relativistic electrons can be described by a power-law distribution, $N(E) = N_0\, E^{-p}$, where N_0 is a constant, $N(E)$ is the number of particles with energy E, and p is the power-law index of the energy spectrum. The energy of a relativistic electron is $E = \gamma m_e c^2$, where γ and m_e are the Lorentz factor and mass of an electron, respectively. For the non-relativistic shock velocities observed in V3890 Sgr, we assume that $E_{\rm min}$ is the rest-mass of the electron ($\gamma_{\rm min} = 1$; Chevalier 1998). The optically thin synchrotron spectrum produced by a power-law distribution of electrons is also a power law, $L_\nu \propto \nu^{-(p-1)/2}$, so that the spectral index $\alpha = -(p-1)/2$. For V3890 Sgr, an average value of $\alpha \approx -0.3$ is measured in the optically thin limit of the radio light curve. This translates to $p = 1.6$. Theoretically, in diffusive shock acceleration, the spectral index of relativistic particles p is predicted to be between 2 and 2.5 (Bell 1978; Blandford & Ostriker 1978). However, for novae, p is observed in the range of 1.2 and 2 (Eyres et al. 2009; Finzell et al. 2018; Nyamai et al. 2021). This could imply a shallower electron energy distribution, or the magnetic fields and particle density are not uniformly distributed leading to complex optical depth effects (Vlasov, Vurm & Metzger 2016). The post-shock energy density is described as $U_{\rm shock} \approx \rho_{\rm CSM}\, V^2_{\rm shock}$, where $\rho_{\rm CSM}$ is the density of the material being shocked and $V_{\rm shock}$ is the velocity of the forward shock. In Chevalier's model, it is assumed that a fraction of the post-shock energy density is transferred to the accelerated electrons and the amplified magnetic field. Therefore, the energy density in relativistic electrons is $U_e = \epsilon_e\, \rho_{\rm CSM}\, V^2_{\rm shock}$ and the energy density in the magnetic field is $U_B = \epsilon_B\, \rho_{\rm CSM}\, V^2_{\rm shock}$. The efficiency factors ϵ_e and ϵ_B are used to describe the fraction of the post-shock energy in the form of relativistic electrons and amplified magnetic fields, respectively. The normalization for the electron energy spectrum can be expressed as follows:

$$N_0 = \epsilon_e\, \rho_{\rm CSM}\, V^2_{\rm shock}\, (p-2)\, E^{p-2}_{\rm min} \tag{2}$$

in cgs units; this expression is valid for $p > 2$.

Chevalier (1998) expresses the flux density of synchrotron emission at frequency ν as follows:

$$S_\nu = 1.8 \times 10^{-22} \left(\frac{\pi\, R^2}{D^2}\right) \frac{C_5}{C_6}\, B^{-0.5}\, \nu^{2.5} \left(1 - \exp\left[-\left(\frac{\nu}{\nu_1}\right)^{\frac{-p-4}{2}}\right]\right) \text{mJy}. \tag{3}$$

Constants C_5 and C_6 are determined as a function of p (Pacholczyk 1970). For V3890 Sgr, we take $p = 2.1$ as this modelling formalism requires $p > 2.1$. Therefore, the values $C_5 = 1.37 \times 10^{-23}$ and $C_6 = 8.61 \times 10^{-41}$ for $p = 2.1$ are used here. R is the radius of the blast wave and D is the distance to the nova. B is the post-shock magnetic field strength and is given by $B = \sqrt{8\,\pi\, U_B}$. ν_1 is the frequency at which the optical depth to synchrotron self-absorption (SSA) is equal to unity, given as

$$\nu_1 = 1.3 \times 10^{19} \times \left(\frac{4}{3} f\, R\, C_6\, N_0\right)^{\frac{2}{p+4}} \times B^{\left(\frac{p+2}{p+4}\right)} \text{Hz}.$$

The synchrotron emitting region is assumed to be between the forward shock and the contact discontinuity; its volume-filling factor is quantified as f. We estimate the value of $f = 0.88$ using the approximations of the forward shock radius and the contact discontinuity radius given in Tang & Chevalier (2017). Based on the authors' approximations, the forward shock radius is twice that of the contact discontinuity.

Radio synchrotron luminosity may increase at early times due to decrease in SSA or free–free absorption by the ionized gas ahead of the forward shock, depending on the amplified magnetic field, the density of the external medium, and the shock wave velocity (Weiler et al. 1986; Chevalier 1998). It has been shown that free–free absorption is dominant for slow shock wave velocities ($\lesssim 10^4$ km s^{-1}), while SSA is the dominant source of opacity for faster blast waves (Chevalier 1998; Panagia et al. 2006). In cases where the optical depth is dominated by an ionized wind-like medium (as described in Section 3.3.2) ahead of the shock, the free–free optical depth is defined by Chevalier (1981) as

$$\tau_{\rm ff} = 0.005 \left(\frac{\dot{M}}{10^{-6}\ \text{M}_\odot\ \text{yr}^{-1}}\right)^2 \times \left(\frac{V_{\rm wind}}{10\ \text{km s}^{-1}}\right)^{-2} \times \left(\frac{\nu}{1.4\ \text{GHz}}\right)^{-2} \times \left(\frac{R_{\rm shock}}{2 \times 10^{16}\ \text{cm}}\right)^{-3}. \tag{4}$$

3.3 The dynamics of the blast wave

To predict the radio luminosity of a nova interacting with circumbinary material, we must know the radius and velocity of the blast

wave. These depend on the density and velocity structure of the nova ejecta, along with the density profile of the circumbinary material.

3.3.1 *The density structure of the nova ejecta*

The unshocked material of the nova envelope is commonly described as expanding freely and homologously, such that $V(r) \propto r$ where V is the expansion velocity and r is the radial distance from the white dwarf. In this case, the ejecta would show a range of velocities with the inner ejecta characterized by low velocities and the outer ejecta expanding fastest. Based on the modelling of nova remnants, the density profiles of the ejecta can be described by a power-law distribution, $\rho_{\rm ej} \propto r^{-n}$ with inner ejecta having $n = 2$ or 3 and outer ejecta having n between 10 and 20 (e.g. Hauschildt et al. 1997). Only a tiny fraction of the ejecta mass is found in the outer parts characterized by a steep power law (and this mass will be swept up very quickly, in just a few hours), so a shallow power law is adopted to describe the ejecta density profile of V3890 Sgr, such that $n = 2$. The kinetic energy of the nova ejecta is, therefore, the integral of the density profile with a homologous expansion such that

$$E = 0.17 \times \left(\frac{M_{\rm ej}}{\rm M_\odot}\right) \times \left(\frac{V_{\rm max}^3}{\rm cm\ s^{-1}} - \frac{V_{\rm min}^3}{\rm cm\ s^{-1}}\right) / \left(\frac{V_{\rm max}}{\rm cm\ s^{-1}} - \frac{V_{\rm min}}{\rm cm\ s^{-1}}\right)^{-1} \rm erg, \quad (5)$$

where $M_{\rm ej}$ is the mass of the nova ejecta, $V_{\rm max}$ is the maximum ejecta velocity, and $V_{\rm min}$ is the minimum ejecta velocity.

Observationally, the ejected masses of symbiotic recurrent novae are in the range of 10^{-7}–10^{-6} $\rm M_\odot$ (O'Brien, Bode & Kahn 1992; Anupama & Sethi 1994; Sokoloski et al. 2006; Orlando, Drake & Miceli 2017). After the 1990 eruption of V3890 Sgr, the optical light curve at V band declined by three magnitude in 14 days (Schaefer 2010). After the 2019 eruption, the optical light curve also shows a fast decline (see Fig. 1). Such a fast decline is expected for nova envelopes with mass of $< 10^{-6}$ $\rm M_\odot$ (Yaron et al. 2005). Furthermore, the same rapid decay of the optical light curve is observed in RS Oph, where its ejected nova envelope is estimated to be ($10^{-7} \leq M_{\rm ej} \leq 10^{-6}$) $\rm M_\odot$ (e.g. O'Brien et al. 1992; Sokoloski et al. 2006). More evidence of a low-mass ejected envelope in V3890 Sgr is based on the fast nova evolution where high-ionization lines appear in the spectra ≈18 days following the 1990 eruption (Anupama & Sethi 1994). Anupama & Sethi use Balmer emission line fluxes to estimate the mass of the nova envelope as $\approx 10^{-7}$ $\rm M_\odot$. In addition, Evans et al. (2022) used Paschen emission line fluxes to estimate the mass of the ejected envelope following the 2019 eruption as 5×10^{-7} $\rm M_\odot$. In our analysis, we consider ejecta masses in the range of 10^{-7}–10^{-5} $\rm M_\odot$.

3.3.2 *The density structure of the circumstellar medium*

The simplest model for the circumstellar material is to assume the companion star is expelling a spherically symmetric wind with constant velocity and mass-loss rate. The density distribution of the medium is then described as

$$\rho_{\rm CSM} = \frac{\dot{M}}{4\pi V_{\rm wind}} r^{-2}, \quad (6)$$

where $\dot{M}$ is the mass-loss rate, $V_{\rm wind}$ is the velocity of the red giant wind, and r is the distance from the companion binary. Without prior knowledge of the distribution of circumstellar material, this spherical distribution of the red giant wind is assumed for V3890 Sgr. It is, however, noted that non-spherical distribution of material is common in symbiotic recurrent systems (Walder, Folini & Shore 2008; Booth, Mohamed & Podsiadlowski 2016a). Furthermore, the two components observed in the emission-line profiles of V3890 Sgr following the 1990 and 2019 eruptions indicate that the nova remnant is non-spherical (Anupama & Sethi 1994; Evans et al. 2022). A spherical assumption considered here is, therefore, a simplistic approach.

3.3.3 *Radius and velocity of the shock front*

The time evolution of a shock wave propagating through the red giant wind is divided into two phases. During the first phase, when the mass of the nova envelope ($M_{\rm ej}$) is much larger than that of the swept-up surrounding medium ($M_{\rm sw}$), the shock is in free expansion. As the mass of the swept-up material increases, such that $M_{\rm sw} > M_{\rm ej}$, the nova envelope enters a second phase of evolution referred to as the Sedov–Taylor phase. For spherical nova ejecta with a power-law density profile ($\rho_{\rm ej} \propto r^{-2}$) interacting with circumstellar medium of density, $\rho_{\rm CSM} \propto r^{-2}$, self-similar solutions are determined for the evolution from a free expansion phase to the adiabatic expansion phase, as shown in Table 1 of Tang & Chevalier (2017). For the purposes of this analysis, we assume that the red giant and white dwarf are co-located at the centre of the red giant wind, a valid assumption over the course of the radio light curve because the shocked ejecta expand outside the binary system within the first day of eruption.

Tang & Chevalier (2017) present expressions for the radius and velocity of the forward shock with time, given as $R_{\rm shock} = R_{ch} \times R_b^*$, $V_{\rm shock} = V_{ch} \times V_b^*$, and $t = t_{ch} \times t^*$. Here R_{ch}, V_{ch}, and t_{ch} are the characteristic radius, velocity, and time, respectively, as follows:

$$R_{ch} = 12.9 \times \left(\frac{M_{\rm ej}}{\rm M_\odot}\right) \times \left(\frac{\dot{M}}{10^{-5}\ \rm M_\odot yr^{-1}}\right)^{-1} \times \left(\frac{V_{\rm wind}}{10\ \rm km\ s^{-1}}\right) \rm pc \quad (7)$$

$$t_{ch} = 1772 \times \left(\frac{E}{10^{51}\ \rm erg}\right)^{-0.5} \times \left(\frac{M_{\rm ej}}{\rm M_\odot}\right)^{1.5} \times \left(\frac{\dot{M}}{10^{-5}\ \rm M_\odot yr^{-1}}\right)^{-1} \left(\frac{V_{\rm wind}}{10\ \rm km\ s^{-1}}\right) \rm yr \quad (8)$$

$$v_{ch} = 7118.24 \times \left(\frac{E}{10^{51}\ \rm erg}\right)^{0.5} \times \left(\frac{M_{\rm ej}}{M_\odot}\right)^{-0.5} \rm km\ s^{-1}. \quad (9)$$

R_b^* and V_b^* are analytical dimensionless quantities defined by Tang & Chevalier (2017), and can be written as a function of $t^* = t/t_{ch}$ as follows:

$$R_b^* = 2.91489 \times t^* \left(1 + 9.36843 t^{*0.567}\right)^{-0.5882} \quad (10)$$

$$V_b^* = \frac{dR^*}{dt^*} = \left(2.91489 + 18.2 t^{*0.567}\right) \left(1 + 9.36843 t^{*0.567}\right)^{-1.5882}. \quad (11)$$

The predicted radius ($R_{\rm shock}$) and velocity ($V_{\rm shock}$) of the blast wave are shown in Fig. 6. The radius and velocity of the shock depend on the ejecta mass (≈10^{-5}–10^{-7} $\rm M_\odot$) and kinetic energy of the nova ejecta, along with the density of the circumbinary material (i.e. $\dot{M}/V_{\rm wind}$). The shock radius first grows linearly with t and later as $t^{0.67}$. Similarly, the shock wave velocity first remains at a near-constant value but decreases as $t^{-0.33}$ at later times. The flux densities depend not only on these quantities, but also on the distance to the nova, ϵ_e and ϵ_B. For a given $M_{\rm ej}$, we iterate to find which E yields maximum expansion velocities at early times (i.e. during free expansion; Fig. 6) consistent with the maximum ejecta velocity of ≈4200 km $\rm s^{-1}$, as estimated from optical spectroscopy (Strader et al. 2019).

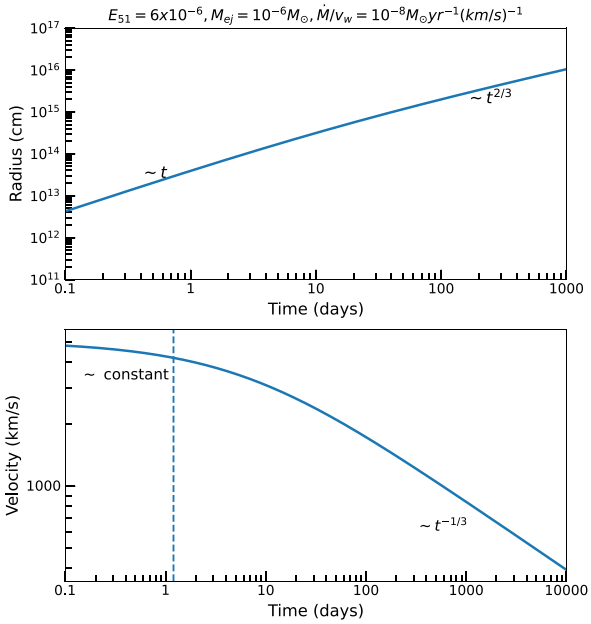

Figure 6. Top: Radial evolution for a nova forward shock interacting with a circumstellar material, assuming ejecta mass of 10^{-6} M$_\odot$, kinetic energy $E = 6 \times 10^{45}$ erg and $\dot{M} = 10^{-7}$ M$_\odot$ yr^{-1} for $V_{\rm wind} = 10$ km s^{-1}. This represents the free expansion ($R_{\rm shock} \propto t$) and the Sedov–Taylor phase of the evolution ($R_{\rm shock} \propto t^{2/3}$). Bottom: Velocity evolution of the forward shock as it interacts with the surrounding medium. At the beginning of the evolution, during the free expansion phase, the velocity is constant. Later, the shock enters the Sedov–Taylor phase of evolution and $V_{\rm shock} \propto t^{-1/3}$. The vertical dashed line represents the initial maximum velocity of ≈4200 km s^{-1} of the nova ejecta on day 1.2 after the nova eruption.

3.4 Modelling the radio light curve of V3890 Sgr

3.4.1 Constraining the mass of the ejected envelope

The radio light curve of V3890 Sgr is compared to the model used to explain non-thermal emission in supernova explosions (Section 3.2; Chevalier 1998). The model depends on various input parameters, including: $p = 2.1$, $V_{\rm wind} = 10$ km s^{-1}, and the distance to the nova (9 kpc). The velocity and radial profile of the expanding material are as discussed in Section 3.3.3.

First, we consider a range of $M_{\rm ej}$ between $M_{\rm ej} = 10^{-5}$ M$_\odot$ and 10^{-7} M$_\odot$. Fig. 7 shows model radio light curves for three different ejecta masses: $M_{\rm ej} = 10^{-5}$ M$_\odot$, 10^{-6} M$_\odot$, and 10^{-7} M$_\odot$. In all three cases, we assume $\dot{M} = 3.2 \times 10^{-8}$ M$_\odot$ yr^{-1} for $V_{\rm wind} = 10$ km s^{-1}. By studying supernova shocks, Chevalier & Fransson (2006), established that microphysical shock parameters $\epsilon_e = \epsilon_B = 0.1$. Similar values are derived from simulations of relativistic shocks (Sironi, Keshet & Lemoine 2015). However, observations of shocks in novae at γ-ray wavelengths determine $\epsilon_e = 0.01$ (Chomiuk, Metzger & Shen 2021a) and simulations of non-relativistic shocks show $\epsilon_B \approx 0.01$ (Caprioli & Spitkovsky 2014). For our fiducial $M_{\rm ej}$ value of 10^{-6} M$_\odot$, we find $\dot{M}$ that produces the radio light curve. Model A and C are demonstrating what happens when we change $M_{\rm ej}$. For a particular value of $M_{\rm ej}$, the kinetic energy is chosen to yield a maximum velocity of ≈4200 km s^{-1} on day 1.2, see Fig. 6. Model parameters are listed in Table 4. For model A (left panel of Fig. 7), the synchrotron emission is significantly more luminous and longer lasting than the observations. With the parameters given in model B in Table 4, $M_{\rm ej} = 10^{-6}$ M$_\odot$ agrees well with the data during the rise and peak of the radio emission (middle panel of Fig. 7). For model C, the right panel of Fig. 7, the radio light curve is less bright and the radio emission does not last very long. None of the models predict the decay phase of the radio light curve accurately. A discussion of why this is the case is included in Section 3.4.2.

For the more massive ejection ($M_{\rm ej} = 10^{-5}$ M$_\odot$) to not overpredict the radio flux densities, the model would require less energy in accelerated particles and amplified magnetic fields, such that $\epsilon_e = \epsilon_B = 0.004$. This is consistent with estimates of particle acceleration implied by modelling of γ-ray emission from a symbiotic nova (e.g. Abdo et al. 2010). Additionally, Sarbadhicary et al. (2017) have also shown ϵ_e to be lower than 0.01 in non-relativistic shocks. Adopting these values of ϵ_e and ϵ_B produces a model D shown in Fig. 8 and tabulated in Table 4.

For the less massive ejection ($M_{\rm ej} = 10^{-7}$ M$_\odot$) to not underpredict the radio flux densities, the model requires a high efficiency of either accelerating particles or amplifying magnetic fields, if not both. As ϵ_B is the more poorly constrained parameter (e.g. Chevalier & Fransson 2006; Lundqvist et al. 2020), we let it vary while holding ϵ_e fixed, finding a good match to the observed light curve with $\epsilon_e = 0.01$ and $\epsilon_B = 0.1$ (Fig. 9; Model E in Table 4). This produces a better fitting model compared to model C. However, since ϵ_B has been shown to vary significantly with values as low as 3×10^{-3} (Lundqvist et al. 2020), this less massive ejection model should be considered with caution.

The most likely mass of the ejecta envelope is, therefore, between 10^{-5} M$_\odot$ and 10^{-6} M$_\odot$. These values of ejecta mass are similar to those estimated in recurrent novae T Pyx (Nelson et al. 2014) and RS Oph (Pandey et al. 2022).

The model of the first radio peak is compared to the VLA radio light curves at frequencies between 1.78 GHz and 7 GHz as shown in Fig. 10.

At higher frequencies, the ejected material becomes optically thin faster and a line of sight can penetrate deeper into the ejecta (compared to observations at lower frequencies), thus providing information at smaller radii. By keeping the ejected mass and $\dot{M}$ at constant values of 10^{-6} M$_\odot$ and $\dot{M} = 3.2 \times 10^{-8}$ M$_\odot$ yr^{-1}, the MeerKAT model does not provide proper fits for any of the VLA radio light curves (see Fig. 10). This implies that the CSM profile cannot be described with $\rho_{CSM} \propto r^{-2}$ at the regions closest to the compact object.

Even though the prediction of synchrotron luminosity is sensitive to the assumptions made, in all the cases presented above, the radio light curve provides an estimate of the mass-loss rate of the red-giant companion of 3.2×10^{-8} M$_\odot$ yr^{-1}, taking the velocity of the red giant wind as 10 km s^{-1}. Using radio observations and assuming spherically distributed ionized circumstellar material in symbiotic systems, Seaquist & Taylor (1990) determined $\dot{M}_{wind} = 10^{-7}$ M$_\odot$ yr^{-1} for most red giant stars assuming $V_{\rm wind} = 10$ km s^{-1}. However, studies of the most studied recurrent nova RS Oph imply a mass-loss rate of 10^{-8} M$_\odot$ yr^{-1} (Vaytet, O'Brien & Bode 2007; Van Loon 2008). The mass-loss rate of V3890 Sgr estimated from its radio light curve is in the range of those found for red giants in symbiotic systems and RS Oph.

3.4.2 Explaining the second radio light curve peak

Although the early shape of the MeerKAT 1.28 GHz radio light curve can be described with a simple model of a $\rho_{CSM} \propto r^{-2}$ circumstellar medium, the light curve then plateaus around days ∼30–60, in excess

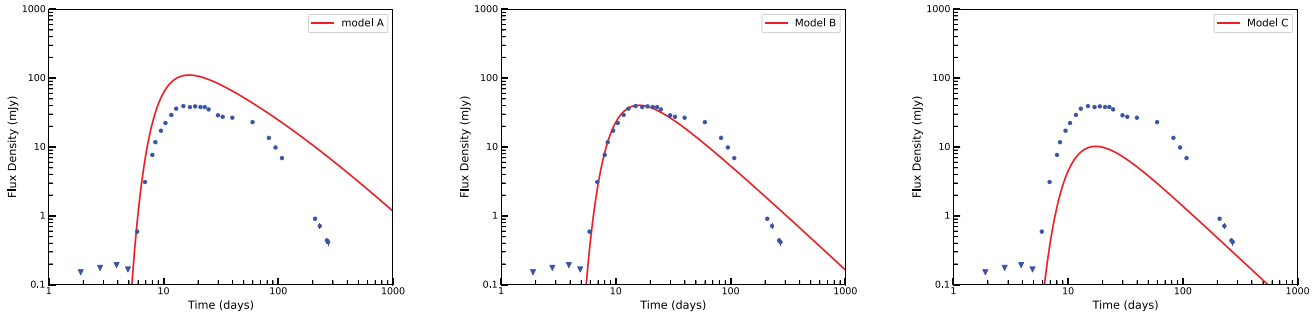

Figure 7. Models of radio emission produced by synchrotron emission undergoing free–free absorption are represented as red solid lines and superimposed on the MeerKAT 1.28 GHz light curve of V3890 Sgr (blue points). The three panels correspond to different models as described in Table 4. For a particular value of $M_{\rm ej}$, the kinetic energy is varied to yield a maximum velocity on day 1.2. For model A (left panel) with $M_{\rm ej} = 10^{-5}$ M$_\odot$, the synchrotron emission is significantly more luminous and longer lasting than the observations. The middle plot shows model B for $M_{\rm ej} = 10^{-6}$ M$_\odot$ and is a good match to the observations during the rise and peak of the radio emission. The right plot represents model C for $M_{\rm ej} = 10^{-7}$ M$_\odot$ and is not luminous enough to match the observations.

Table 4. Model parameters.

Model	Frequency (GHz)	Kinetic energy (erg)	Ejecta mass (M$_\odot$)	ϵ_e	ϵ_B	RG wind $\dot{M}$ (M$_\odot$ yr^{-1})
A	1.28	4.5×10^{44}	10^{-5}	0.01	0.01	3.2×10^{-8}
B	1.28	6.0×10^{43}	10^{-6}	0.01	0.01	3.2×10^{-8}
C	1.28	1.4×10^{43}	10^{-7}	0.01	0.01	3.2×10^{-8}
D	1.28	4.5×10^{44}	10^{-5}	0.004	0.004	3.2×10^{-8}
E	1.28	1.4×10^{43}	10^{-7}	0.01	0.1	3.2×10^{-8}
F	1.78, 5.0, 7.0	6.0×10^{43}	10^{-6}	0.01	0.01	3.2×10^{-8}

Note. Here we assume a wind velocity, $V_{\rm wind} = 10$ km s^{-1}.

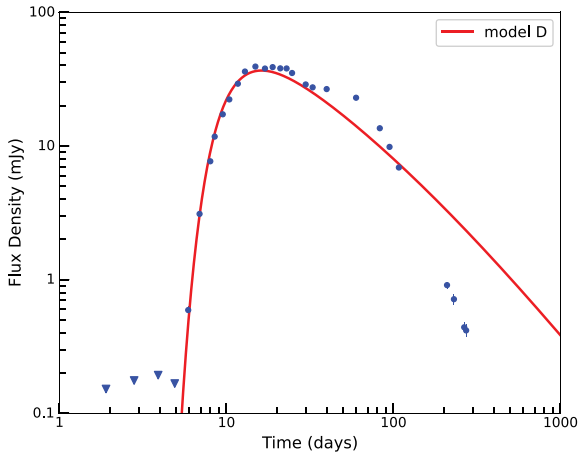

Figure 8. Model of radio emission produced by synchrotron emission undergoing free–free absorption (represented as the red solid line), superimposed on the MeerKAT light curve (blue points) for a massive ejection $M_{\rm ej} = 10^{-5}$ M$_\odot$ with a shock that is less efficient at accelerating electrons and amplifying magnetic fields; see model D in Table 4 for details.

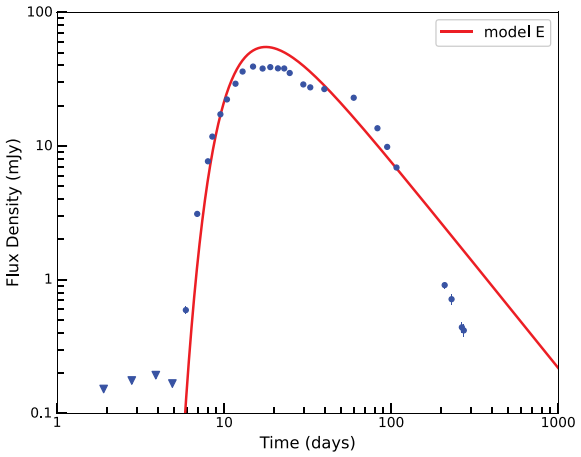

Figure 9. Model of radio emission produced by synchrotron emission undergoing free–free absorption represented (red solid line) superimposed on the MeerKAT light curve (blue points) for a less massive ejection $M_{\rm ej} = 10^{-7}$ M$_\odot$ that is more efficient at amplifying the post-shock magnetic field; see model E in Table 4 for details.

of the model (Figs 7–10; see also Fig. 2). We call this excess emission the 'second peak' of the radio light curve.

Before day 17, the radio flux is rising. During the decay phase of the radio light curve of V3890 Sgr, the flux densities can be described by a power-law relationship with time such that $S_\nu \propto t^\beta$. Between days 17 and 40, the radio emission flattens such that $\beta = -0.5$. After the second peak, from day 60 onwards, the radio flux density rapidly declines as $\beta = -2.8$, which is a steeper decay than predicted by our model with a $\rho_{CSM} \propto r^{-2}$ circumstellar medium. This standard model is described by $\beta = -1.3$ for the decline phase (Chevalier & Fransson 2006). The synchrotron luminosity produced when a nova remnant interacts with the circumstellar medium is expected to rise, peak, and decay in a span of a few months (Kantharia et al. 2016). The radio luminosity in this framework decays during the optically thin phase of the radio light curve due to a decrease in both the circumbinary density and shock wave velocity (Weiler et al. 2002). The second radio peak we observe cannot be explained by a single interaction with a spherically distributed wind-like circumstellar medium.

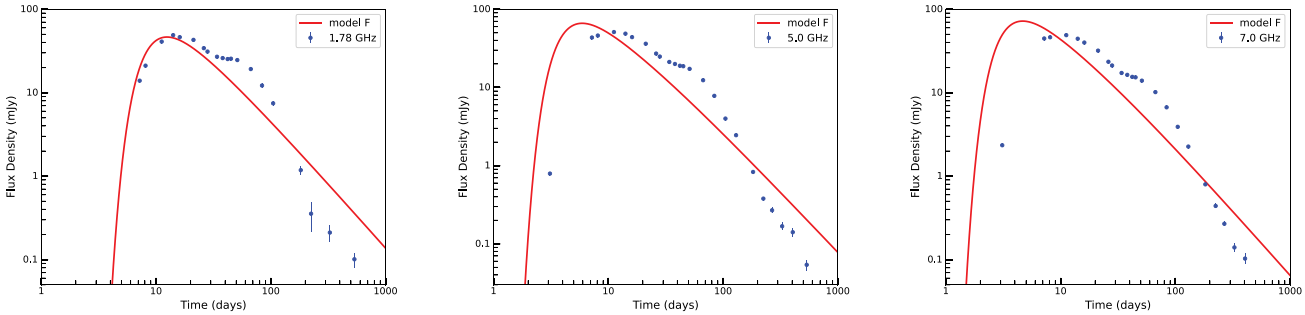

Figure 10. Models of radio emission produced by synchrotron emission undergoing free–free absorption are represented as red solid lines and superimposed on the VLA data (blue points) observed at frequencies 1.78 GHz (left panel), 5.0 GHz (middle), and 7.0 GHz (right). The three panels represent model F (see Table 4).

Double-peaked radio light curves have been observed previously in novae with giant companions, but on different time-scales. For example, the radio light curve of the 2006 eruption of nova RS Oph showed a first peak around day 8, which was followed by a second peak on day 40 (Eyres et al. 2009). Based on its spectral evolution, the authors concluded that the radio emission from the nova is mixed thermal and non-thermal radiation. V1535 Sco is another symbiotic nova where the radio light curve shows several radio peaks with the first one recorded on day 25 (Linford et al. 2017). The spectral evolution of V1535 Sco is also consistent with a mixture of thermal and non-thermal emission (Linford et al. 2017).

V3890 Sgr is the first symbiotic recurrent nova where the second radio bump is clearly dominated by non-thermal emission, given that the spectral index is predominantly negative with values of α ranging between -0.3 and -0.4, see Table 3. The brightness temperature also remains high ($\gtrsim 10^5$ K) even at day 100 (Fig. 5).

So what might explain the second radio peak and the subsequent fast decay of V3890 Sgr? The luminosity remaining bright compared to the model translates to either an excess of shock velocity or an excess density of material being shocked, relative to our simple model. While many novae show multiple ejections and increases in ejecta velocity as an eruption proceeds (Aydi et al. 2020), the fast eruptions of symbiotic recurrent novae can generally be described as a single ejection decelerating as it sweeps up circumstellar material (e.g. Walder et al. 2008; Orlando, Drake & Laming 2009; Munari et al. 2011). We therefore interpret V3890 Sgr's deviations from our simple model as complex structure in the circumstellar material (i.e. the density distribution does not just decrease as r^{-2}, as expected if the red giant companion powered a wind with constant velocity and mass-loss rate).

In fact, it has been shown that the surrounding medium in systems like V3890 Sgr is likely to be structured and aspherical. For example, simulations of RS Oph show that material lost from the companion star ends up concentrated in the orbital plane during the mass transfer process (Walder et al. 2008; Booth, Mohamed & Podsiadlowski 2016b). Mass-loss from the outer Lagrangian points imposes spiral waves on circumstellar material and can create complex structure as the spirals interact. In addition, a non-uniform distribution of material may arise due to changes in the mass-loss rate or wind velocity from the companion star. Finally, recurrent nova eruptions likely sweep up circumstellar material, leading to shells bounded by lower density cavities (Moore & Bildsten 2012; Darnley et al. 2019).

The excess in radio emission between days $\sim$30 and 60 therefore implies a relatively dense 'shell' of CSM at $\sim 10^{15}$ cm from the binary (see the radius evolution in Fig. 6). The rapid decline of the radio light curve after day 60 implies circumstellar material whose density declines more steeply than $\propto r^{-2}$ (see equation 3 in Nyamai et al. 2021), which can be pictured as a lower density region at radii $\gtrsim 1.3 \times 10^{15}$ cm. Similar low-density material at $\approx 10^{15}$ cm is implied in another symbiotic nova V407 Cyg (Chomiuk et al. 2012). While such a shell/cavity structure is tempting to blame on past nova eruptions sweeping up the giant's wind, this is unlikely since the material ejected during V3890 Sgr's 1992 eruption should be at a radii of $\sim 10^{16}$ cm based on Fig. 6. Unless the 1992 eruption was quite different from the 2019 eruption (contrary to the findings of Schaefer 2010, who find that eruptions in the same recurrent nova system generally match each other well), it is difficult to imagine how the 2019 ejecta could 'catch up' to the 1992 ejecta. The most likely cause of the structure in the circumstellar material is, therefore, the mass transfer/accretion process itself (Mohamed & Podsiadlowski 2007; Walder et al. 2008).

Radio observations are not the only evidence for complex structure in the circumstellar material around V3890 Sgr. *Chandra* High Energy Transmission Grating observations of V3890 Sgr on day 7 showed X-ray emission lines that are asymmetric, blue-shifted, and indicating multiple plasma temperatures (Orio et al. 2020). Orio et al. suggest that a non-uniform distribution of the circumbinary medium could be the source of the different emission region temperatures. The Hα emission line of V3890 Sgr obtained using the Asiago 1.22 m telescope shows a broad component observed from day 1 following the 2019 eruption. A narrow component appears at least 13 days after the eruption (Munari & Walter 2019c). This implies presence of both fast and slow outflows of the ejecta. Evolution of emission lines at infrared wavelengths indicates both fast uninterrupted polar outflow and a slow equatorial outflow as a result of encounter with surrounding medium (Evans et al. 2022). Binary interaction simulations of systems similar to V3890 Sgr reveal asymmetries in the distribution of circumbinary material, such that the dense material is concentrated at the orbital plane and the less dense material is concentrated at the polar directions of the binary systems (Booth et al. 2016b). The radio emission is, therefore, possibly originating from the interaction of the shock with dense material. The shock interaction in the equatorial region, therefore, dominates the radio luminosity as the less dense polar outflow expands without much deceleration.

3.5 V3890 Sgr as a progenitor of SNe Ia

The estimated low ejecta mass for the nova envelope (in the range of 10^{-7}–10^{-6} $M_\odot$) and the short recurrence time of 28 years imply that V3890 Sgr hosts a massive white dwarf ($\gtrsim$ 1.2 $M_\odot$, Yaron et al. 2005), making it an interesting candidate for a SN Ia progenitor system. Non-detections of radio emission from SNe Ia have provided an opportunity to rule out candidate single degenerate progenitor systems through comparison of radio models and radio luminosity upper limits (e.g. Panagia et al. 2006; Chomiuk et al. 2016; Lundqvist et al. 2020). The radio observations of SNe Ia that are used to rule out symbiotic systems are typically obtained a few weeks to months after explosion. However, in our analysis of V3890 Sgr, we detect circumstellar material at radii $\lesssim$ few $\times$ 10^{15} cm, with a rapid fall-off in density at larger radii. Such CSM would, therefore, be best constrained if radio observations of SNe Ia were obtained within a $\sim$day following explosion (see equation 10 of Chomiuk et al. 2016).

The only SN Ia with such early radio follow-up published is SN 2011fe, where the first radio observation was obtained 1.4 days after explosion (Horesh et al. 2012, see also Chomiuk et al. 2012). A symbiotic progenitor with a wind mass-loss rate $>2 \times 10^{-8}\ M_\odot\ \mathrm{yr}^{-1}$ is ruled out for SN 2011fe, assuming $\epsilon_e = 0.1, \epsilon_B = 0.01$, and $V_{\rm wind} =$ 10 km s^{-1} (Horesh et al. 2012). This radio limit from 1.4 days after explosion constrains the CSM at a radius of $\sim 1.5 \times 10^{15}$ cm. Given that the radio light curve of V3890 Sgr is well modelled as an r^{-2} stellar wind with $\dot{M} = 3.2 \times 10^{-8}\ M_\odot\ \mathrm{yr}^{-1}$ out to day 30 (shock radius $\sim 8 \times 10^{14}$ cm; Fig. 6) and then a shell of excess CSM density out to day $\sim$100 ($\sim 2 \times 10^{15}$ cm), we can rule out a V3890 Sgr progenitor to SN 2011fe. In the future, such direct comparisons with real-world candidate progenitors can be extended to additional SNe Ia by modelling the blastwave evolution in embedded novae like V3890 Sgr (constrained by optical spectral line profiles) and by scaling up the radio light curves observed for novae to the blastwave energetics expected for SNe Ia.

4 CONCLUSIONS

The symbiotic recurrent nova V3890 Sgr was observed for 18 months at radio frequencies with MeerKAT and the VLA (Fig. 1). The radio emission is detected from 3 days after optical discovery and peaks between days 11 and 15 at all observed frequencies. The rapid time evolution of the radio light curve, steep spectral indices (Fig. 2), and high brightness temperatures (Fig. 5) are indicators of synchrotron radiation from the nova, similar to what is observed in other symbiotic recurrent novae (e.g. Kantharia et al. 2016).

The synchrotron emission in V3890 Sgr is suggested to arise from the interaction between the ejected nova envelope and a structured circumbinary medium formed by the pre-existing wind from the red giant star. The radio light curve is characterized by a secondary peak following the initial peak, and then decays faster than expected for a shock wave propagating in a windlike medium ($\rho_{CSM} \propto r^{-2}$; Fig. 7). This hints at a complex structure of circumstellar medium around the nova, with an excess of material at $\sim 10^{15}$ cm surrounded by a relatively low-density outer environment.

The turn-on of the radio emission fits well with a model of decreasing opacity of the ionized circumstellar gas as the ejected envelope of $\approx 10^{-6}$ $M_\odot$ sweeps through it (Chevalier 1981). Modelling of the radio emission provides a mass-loss rate of the red giant companion star on the order of $\dot{M} = 3.2 \times 10^{-8}\ M_\odot\ \mathrm{yr}^{-1}$ for $V_{\rm wind} = 10\ \mathrm{km\ s}^{-1}$ and a distance of 9 kpc. Similar mass-loss rates are estimated for RS Oph (Van Loon 2008) and other symbiotic stars (Seaquist & Taylor 1990). By comparing our light curve with radio upper limits for SNe Ia, we conclude that a V3890 Sgr-like progenitor can be ruled out for the well-observed SN 2011fe.

ACKNOWLEDGEMENTS

The authors thank the referee for constructive feedback that improved the quality of this work. The MeerKAT telescope is operated by the South African Radio Astronomy Observatory (SARAO; www.ska.ac.za), which is a facility of the National Research Foundation (NRF), an agency of the Department of Science and Innovation. The data were processed using the Ilifu cloud computing facility – www.ilifu.ac.za, a partnership between the University of Cape Town, the University of the Western Cape, the University of Stellenbosch, Sol Plaatje University, the Cape Peninsula University of Technology, and the South African Radio Astronomy Observatory. The Ilifu facility is supported by contributions from the Inter-University Institute for Data Intensive Astronomy (IDIA – https://www.idia.ac.za/ a partnership between the University of Cape Town, the University of Pretoria, and the University of the Western Cape), the Computational Biology division at UCT, and the Data Intensive Research Initiative of South Africa (DIRISA)). This research was supported by SARAO student bursary and in part by the National Science Foundation under Grant No. NSF PHY-1748958. MMN and PAW kindly acknowledge financial support from the University of Cape Town and the NRF Grant 129359 and NRF SARChI Grant 111692. MMN acknowledges the financial support in part by the National Science Foundation under Grant No. NSF PHY-1748958. LC is grateful for NSF support through grants AST-1751874, AST-1907790, and AST-2107070. VARMR acknowledges financial support from the Fundação para a Ciência e a Tecnologia (FCT) in the form of an exploratory project of reference IF/00498/2015/CP1302/CT0001, and supported by Enabling Green E-science for the Square Kilometre Array Research Infrastructure (ENGAGE-SKA), POCI-01-0145-FEDER-022217, funded by Programa Operacional Competitividade e Internacionalização o (COMPETE 2020) and FCT, Portugal. We thank the NRAO for the generous allocation of time on the VLA. The National Radio Astronomy Observatory is a facility of the National Science Foundation operated under cooperative agreement by Associated Universities, Inc.

DATA AVAILABILITY

All MeerKAT data for V3890 Sgr are available from the MeerKAT archive at archive.sarao.ac.za search under the project codes SCI-20190418-MN-01 and DDT-20200323-MN-01. All VLA data for this project are publicly available from the NRAO archive at data.nrao.edu. The project codes were 19A-313 and 20B-302.

REFERENCES

Abdo A. A. et al., 2010, Science, 329, 817
Anupama G. C., Mikołajewska J., 1999, A&A, 344, 177
Anupama G. C., Sethi S., 1994, MNRAS, 269, 105
Aydi E. et al., 2020, ApJ, 905, 62
Buckley D. A. H., Wargau W. F., Soltynski M. G., Shao C. Y., Hazen M. L., 1990, IAU Circ., 5019, 1
Brandi E., Quiroga C., Mikołajewska J., Ferrer O. E., García L. G., 2009, A&A, 497, 815
Banerjee D. P. K., Joshi V., Venkataraman V., Ashok N. M., Marion G. H., Hsiao E. Y., Raj A., 2014, ApJ, 785, L11
Bell A. R., 1978, MNRAS, 182, 147
Bell A. R., 2004, MNRAS, 353, 550
Bode M. F., Kahn F. D., 1985, MNRAS, 217, 205

Blandford R. D., Ostriker J. P., 1978, ApJ, 221, L29
Bode M. F. et al., 2006, ApJ, 652, 629
Booth R. A., Mohamed S., Podsiadlowski P., 2016a, MNRAS, 457, 822
Booth R. A., Mohamed S., Podsiadlowski P., 2016b, MNRAS, 457, 822
Bailer-Jones C. A. L., Rybizki J., Fouesneau M., Mantelet G., Andrae R., 2018, AJ, 156, 58
Buson S., Jean P., Cheung C. C., 2019, Astron. Telegram, 13114, 1
Chevalier R. A., Fransson C., 2006, ApJ, 651, 381
Caprioli D., Spitkovsky A., 2014, ApJ, 783, 91
Chauhan J. et al., 2021, MNRAS, 501, L60
Chevalier R. A., 1981, ApJ, 251, 259
Chevalier R. A., 1982a, ApJ, 258, 790
Chevalier R. A., 1982b, ApJ, 259, 302
Chevalier R. A., 1998, ApJ, 499, 810
Chomiuk L. et al., 2012, ApJ, 750, 164
Chomiuk L. et al., 2016, ApJ, 821, 119
Chomiuk L., Metzger B. D., Shen K. J., 2021a, ARA&A, 59, 391
Chomiuk L. et al., 2021b, ApJS, 257, 49
Darnley M. J. et al., 2019, Nature, 565, 460
Evans A., Geballe T. R., Woodward C. E., Banerjee D. P. K., Gehrz R. D., Starrfield S., Shahbandeh M., 2022, MNRAS, 517, 6077
Eyres S. P. S. et al., 2009, MNRAS, 395, 1533
Finzell T. et al., 2018, ApJ, 852, 108
Gonzalez-Riestra R., 1992, A&A, 265, 71
Greisen E. W., 2003, in Heck A., ed., Astrophysics and Space Science Library, Vol. 285, Information Handling in Astronomy – Historical Vistas. Kluwer Academic Publishers, Dordrecht, p. 109
Gutierrez J., Garcia-Berro E., Iben Icko, J., Isern J., Labay J., Canal R., 1996, ApJ, 459, 701
Green G. M., Schlafly E., Zucker C., Speagle J. S., Finkbeiner D., 2019, ApJ, 887, 93
Hjellming R. M., van Gorkom J. H., Taylor A. R., Sequist E. R., Padin S., Davis R. J., Bode M. F., 1986, ApJ, 305, L71
Harrison T. E., Johnson J. J., Spyromilio J., 1993, AJ, 105, 320
Hauschildt P. H., Shore S. N., Schwarz G. J., Baron E., Starrfield S., Allard F., 1997, ApJ, 490, 803
Hewitt D. M. et al., 2020, MNRAS, 496, 2542
Heywood I., 2020, Astrophysics Source Code Library, record ascl:2009.003
Horesh A. et al., 2012, ApJ, 746, 21
Ji S. et al., 2013, ApJ, 773, 136
Jonas J., MeerKAT Team, 2016, in Proc. MeerKAT Science: On the Pathway to the SKA. Proc. Sci., Stellenbosch. p. 1
Kafka S., 2020, Observations from the AAVSO International Database. https://www.aavso.org
Kaminsky B. et al., 2022, MNRAS, 517, 6064
Kantharia N. G. et al., 2016, MNRAS, 456, L49
Kenyon S. J., Garcia M. R., 1986, AJ, 91, 125
Lallement R., Vergely J. L., Valette B., Puspitarini L., Eyer L., Casagrande L., 2014, A&A, 561, A91
Linford J. D. et al., 2017, ApJ, 842, 73
Luna G. J. M., 2019, Boletin de la Asociacion Argentina de Astronomia La Plata Argentina, 61, 93
Lundqvist P. et al., 2020, ApJ, 890, 159
McMullin J. P., Waters B., Schiebel D., Young W., Golap K., 2007, in Shaw R. A., Hill F., Bell D. J., eds, ASP Conf. Ser.Vol. 376, CASA Architecture and Applications. Astron. Soc. Pac., San Francisco, p.127
Maoz D., Mannucci F., Nelemans G., 2014, ARA&A, 52, 107
Miller L. T. P., 1991, J. Am. Assoc. Var. Star Obs., 20, 182
Moore K., Bildsten L., 2012, ApJ, 761, 182
Mohamed S., Podsiadlowski P., 2007, in Napiwotzki R., Burleigh M. R., eds, ASP Conf. Ser.Vol. 372, Wind Roche-Lobe Overflow: a New Mass-Transfer Mode for Wide Binaries. Astron. Soc. Pac., San Francisco. p. 397
Mohamed S., Booth R., Podsiadlowski P., Ramstedt S., Vlemmings W., Maercker M., 2015, in 3D Models of Symbiotic Binaries. EAS Publications Series, Nice, France, p. 81
Mondal A., Anupama G. C., Kamath U. S., Das R., Selvakumar G., Mondal S., 2018, MNRAS, 474, 4211
Mikołajewska J., Iłkiewicz K., Gałan C., Monard B., Otulakowska-Hypka M., Shara M. M., Udalski A., 2021, MNRAS, 504, 2122
Munari U., 2019, The Symbiotic Stars. Cambridge Univ. Press, Cambridge, p. 77
Mürset U., Schmid H. M., 1999, A&AS, 137, 473
Munari U., Walter F. M., 2019a, Astron. Telegram, 13069, 1
Munari U., Walter F. M., 2019b, Astron. Telegram, 13081, 1
Munari U., Walter F. M., 2019c, Astron. Telegram, 13099, 1
Munari U. et al., 2011, MNRAS, 410, L52
Nelson T. et al., 2014, ApJ, 785, 78
Ness J. U. et al., 2022, A&A, 658, A169
Nyamai M. M., Woudt P. A., Ribeiro V. A. R. M., Chomiuk L., 2019, Astron. Telegram, 13089, 1
Nyamai M. M., Chomiuk L., Ribeiro V. A. R. M., Woudt P. A., Strader J., Sokolovsky K. V., 2021, MNRAS, 501, 1394
O'Brien T. J., Bode M. F., Kahn F. D., 1992, MNRAS, 255, 683
O'Brien T. J. et al., 2006, Nature, 442, 279
Offringa A. R. et al., 2014, MNRAS, 444, 606
Orio M. et al., 2020, ApJ, 895, 80
Orlando S., Drake J. J., Laming J. M., 2009, A&A, 493, 1049
Offringa A. R., van de Gronde J. J., Roerdink J. B. T. M., 2012, A&A, 539, A95
Orlando S., Drake J. J., Miceli M., 2017, MNRAS, 464, 5003
Osborne J. P. et al., 2011, ApJ, 727, 124
Pacholczyk A. G., 1970, Radio Astrophysics: Nonthermal Processes in Galactic and Extragalactic Sources, A Series of Books in Astronomy and Astrophysics. W. H. Freeman, San Francisco
Page K. L. et al., 2015, MNRAS, 454, 3108
Page K. L. et al., 2020, MNRAS, 499, 4814
Panagia N., Van Dyk S. D., Weiler K. W., Sramek R. A., Stockdale C. J., Murata K. P., 2006, ApJ, 646, 369
Pandey R., Habtie G. R., Bandyopadhyay R., Das R., Teyssier F., Guarro Fló J., 2022, MNRAS, 515, 4655
Payne-Gaposchkin C., 1964, The Galactic Novae, Dover Books on Astronomy and Astrophysics. Dover Publications, New York
Polisensky E. et al., 2019, Astron. Telegram, 13185, 1
Prialnik D., Kovetz A., 1995, ApJ, 445, 789
Rupen M. P., Mioduszewski A. J., Sokoloski J. L., 2008, ApJ, 688, 559
Reynolds S. P., 2017, Dynamical Evolution and Radiative Processes of Supernova Remnants. Springer International Publishing, Cham, p. 1981
Shepherd M. C., 1997, in Hunt G., Payne H., eds, ASP Conf. Ser.Vol. 125, Difmap: An Interactive Program for Synthesis Imaging. Astron. Soc. Pac., San Francisco, p. 77
Schaefer B. E., 2009, ApJ, 697, 721
Schaefer B. E., 2010, ApJS, 187, 275
Stanishev V., Zamanov R., Tomov N., Marziani P., 2004, A&A, 415, 609
Seaquist E. R., Taylor A. R., 1990, ApJ, 349, 313
Sokoloski J. L., Luna G. J. M., Mukai K., Kenyon S. J., 2006, Nature, 442, 276
Sokoloski J. L., Rupen M. P., Mioduszewski A. J., 2008, ApJ, 685, L137
Sironi L., Keshet U., Lemoine M., 2015, Space Sci. Rev., 191, 519
Sarbadhicary S. K., Badenes C., Chomiuk L., Caprioli D., Huizenga D., 2017, MNRAS, 464, 2326
Singh K. P., Girish V., Pavana M., Ness J.-U., Anupama G. C., Orio M., 2021, MNRAS, 501, 36
Sokolovsky K. V. et al., 2019, Astron. Telegram, 13050, 1
Strader J. et al., 2019, The Astronomer's Telegram, 13047, 1
Tang X., Chevalier R. A., 2017, MNRAS, 465, 3793
Taylor A. R., Davis R. J., Porcas R. W., Bode M. F., 1989, MNRAS, 237, 81
Van Loon J. T., 2008, in Evans A., Bode M. F., O'Brien T. J., Darnley M. J., eds, ASP Conf. Ser.Vol. 401, RS Ophiuchi (2006) and the Recurrent Nova Phenomenon. Astron. Soc. Pac., San Francisco, p. 90 preprint (arXiv:0710.5628)
Vaytet N. M. H., O'Brien T. J., Bode M. F., 2007, ApJ, 665, 654
Vlasov A., Vurm I., Metzger B. D., 2016, MNRAS, 463, 394
Weiler K. W., Sramek R. A., Panagia N., van der Hulst J. M., Salvati M., 1986, ApJ, 301, 790

Weiler K. W., Panagia N., Montes M. J., Sramek R. A., 2002, ARA&A, 40, 387
Walder R., Folini D., Shore S. N., 2008, A&A, 484, L9
Wolf W. M., Bildsten L., Brooks J., Paxton B., 2013, ApJ, 777, 136
Wenger T. V., Balser D. S., Anderson L. D., Bania T. M., 2018, ApJ, 856, 52
Wenzel W., 1990, Inf. Bull. Var. Stars, 3517, 1
Yaron O., Prialnik D., Shara M. M., Kovetz A., 2005, ApJ, 623, 398
Zheng J.-H., Huang Y.-Y., Zhang Z.-L., Zhang H.-M., Liu R.-Y., Wang X.-Y., 2022, Phys. Rev. D, 106, 103011, preprint (arXiv:2203.16404)

This paper has been typeset from a TEX/LATEX file prepared by the author.